J Therm Spray Tech (2025) 34:1589–1597
https://doi.org/10.1007/s11666-025-02003-6

ORIGINAL RESEARCH ARTICLE

Localized Phase and Elemental Mapping in Solid-State Lithium Battery LTO Anode Thin-Film Produced by a Novel Suspension Plasma Spray Approach

Arman Hasani[1] · Shrikant Joshi[2] · Antti Salminen[1] · Sneha Goel[3] · Joakim Reuteler[4] · Malgorzata Grazyna Makowska[5] · Ashish Ganvir[1]

Submitted: 20 November 2024 / in revised form: 14 March 2025 / Accepted: 8 April 2025 / Published online: 8 May 2025

Abstract This study investigates the phase and elemental distribution in a suspension plasma-sprayed (SPS) $Li_4Ti_5O_{12}$ (LTO) thin-film anode for solid-state lithium batteries, deposited on an SS-304 substrate. Advanced synchrotron-based μXRD and μXRF techniques were employed for micro-scale characterization, revealing distinct phase regions influenced by thermal exposure during the SPS process. The dominant $Li_4Ti_5O_{12}$ phase was retained across most of the film, with localized transformations to secondary phases $Li_2Ti_3O_7$, Li_2TiO_3, and TiO_2 near the substrate interface, primarily due to prolonged high-temperature exposure and subsequent lithium loss. These findings underscore the importance of controlling SPS parameters to minimize lithium loss and optimize phase stability and interfacial integrity in solid-state battery components.

Keywords focused ion beam milling · LTO thin-film ceramic solid-state battery electrode · suspension plasma spraying · synchrotron micro-x-ray diffraction and micro-x-ray fluorescence · thin films

✉ Arman Hasani
arman.hasani@utu.fi

[1] Department of Mechanical and Materials Engineering, Faculty of Technology, University of Turku, Turku, Finland

[2] Department of Engineering Science, University West, Trollhättan, Sweden

[3] Advanced Materials for Nuclear Energy, VTT Technical Research Centre of Finland, Espoo, Finland

[4] Scientific Center for Optical and Electron Microscopy, ETH Zürich, Zurich, Switzerland

[5] Laboratory for Synchrotron Radiation and Femtochemistry and Laboratory for Nuclear Materials, Advanced Nuclear Materials Group, Paul Scherrer Institute, 5232 Villigen PSI, Switzerland

Introduction

Solid-state batteries (SSBs), harnessing the potential of ceramic fast ion conductors, are widely acclaimed for their exceptional attributes, including high energy density, enhanced power density, safety, a broad electrochemical stability window, lack of electrolyte leakage, and extended cycle life (Ref 1-3). The diverse inorganic materials contributing to state-of-the-art SSBs encompass solid electrolytes, cathode, and anode like $Li_4Ti_5O_{12}$ (LTO). Within the pseudo-binary Li_2O–TiO_2 system for LTO, $Li_4Ti_5O_{12}$ stands out for battery applications due to its excellent cycling performance and long life in the cubic spinel structure (Ref 4-8).

Advanced production methods like pulsed laser deposition (PLD), chemical vapor deposition (CVD), and electrostatic spray deposition are used to fabricate high-quality thin-film battery components. While effective, these methods are complex, costly, and have slow deposition rates. In contrast, suspension plasma spraying (SPS) offers a simpler, cost-effective, and industrially viable alternative for producing thin-film SSBs (Ref 9-12).

In SPS, ceramic or metallic powders suspended in a liquid medium are sprayed into a plasma plume from a plasma spray torch. The suspension stream is atomized into fine droplets due to atomization gas and further into finer droplets by viscous thermal-plasma (plasma plume temperature typically ranges from 10,000 to 15,000 °C) (Ref 13) where the liquid medium (solvent) is evaporated first, and the remnant solute particles then partially or fully melt in-flight before impacting the substrate to form a thin

coating by rapid quenching in a layer-by-layer fashion. The cooling rates in plasma spraying can range from 10^4 to 10^9 Kelvin per second (K/s) (Ref 14, 15). The detailed mechanism of coating formation in SPS, involving the injection of suspension into plasma, is described by Ganvir et al. (Ref 16). Process parameters like plasma gas flow rate, suspension feed rate, spray distance, etc. are known to considerably influence coating properties (Ref 17). SPS processing is ideal for manufacturing thin-film solid-state batteries, enabling rapid fabrication of films with tailored microstructures and controlled porosity over large areas (Ref 16). A key challenge in using SPS for thin-film SSBs is creating solid-solid interfaces with sufficient integrity, as SPS coatings depend on mechanical anchoring for bonding. Additionally, the extreme heat from plasma can degrade and decompose LTO phases, alter their chemistry, and cause elemental interdiffusion between the ceramic anode and metallic current collector. Decomposition of the spinel phase LTO ($Li_4Ti_5O_{12}$) to Lithium meta-titanate (Li_2TiO_3) and Ramsdellite ($Li_2Ti_3O_7$) is a common phenomenon reported at temperatures above 1015 °C (Ref 18, 19).

On the other hand, since the plasma spraying is a high-temperature production method, in order to avoid undesired interdiffusion and partial lithium deintercalation which could affect the efficiency of the SSB-based LTO, there are several strategies can be employed to reduce the temperature and, consequently, minimize interdiffusion and partial lithium deintercalation. Potential solutions to mitigate interdiffusion and partial lithium deintercalation include process optimization, the application of a barrier layer, the use of lithium-rich precursors, atmosphere control, and exploring low-temperature deposition methods. Adjusting plasma spray parameters—such as enthalpy and spray distance—can help minimize prolonged high-temperature exposure. Additionally, injecting the suspension radially instead of axially may reduce lithium loss and phase transformation. Controlling the quenching rate, for example, through controlled substrate cooling, could further aid in retaining the desired phase (Ref 20-23). Introducing a thin diffusion barrier coating (e.g., TiN, SiO_2, Al_2O_3, ZrO_2, TiO_2, $BaTiO_3$, etc.) between the LTO film and SS-304 to suppress Fe, Cr, Ni, and Mn interdiffusion. This is a common approach in high-temperature systems to improve stability (Ref 24-26). If it is necessary to compensate for the lithium loss during the plasma spraying process, it is possible to use Lithium-rich precursors. It means using a slightly Li-enriched suspension feedstock could compensate for lithium loss during plasma spraying, ensuring better phase stability and reducing unwanted phase formation. Additionally, atmosphere control can be another solution. If feasible, adjusting the plasma gas composition (e.g., adding a reducing component like H_2/Ar) could help mitigate Ti oxidation and maintain the original LTO stoichiometry (Ref 27, 28). Finally, exploring alternative thermal spraying methods would be an alternative for high-temperature plasma spraying. Techniques like flame spraying, in particular, offer a promising approach for depositing a thin, dense, and reliable LTO coating while mitigating interdiffusion and lithium deintercalation. This is an area we are currently investigating.

Therefore, characterizing the SPS-deposited LTO anode thin-film on a metallic current collector is crucial for understanding phase and elemental composition within the film and across the anode-current collector interface. Due to inherent heterogeneity, localized micro-scale characterization is needed to understand chemistry variations, especially in the narrow interface region. Traditional bulk characterization methods are unable to capture variations in structures such as phase composition and chemistry at the microscale. Microscale characterization of SSB components is particularly informative. Techniques like SPS, which inherently introduces structural heterogeneity, are especially relevant for this analysis. In this context, Synchrotron micro XRD/XRF (hereafter μXRD/μXRF) is a technique that allows for micro-scale localized characterization of material structure. The μXRD/μXRF scanning imaging is a non-destructive technique that provides information on the spatial distribution of chemical elements and crystalline phases present (Ref 29, 30). Therefore, in this work, the above techniques were explored to study the solid-solid interfacial regions in the SPS-produced thin-film SSB LTO anode deposited on the SS-304 substrate.

Experimental Works

Coating material and deposition process: Lithium Titanium Oxide powder, $Li_4Ti_5O_{12}$ (LTO) from NEI Corporation, USA, was utilized, featuring an average particle size of 1.5-3 micrometers. A disk-shaped Stainless Steel 304 (SS-304) substrate with a diameter of 25 mm and a thickness of 2 mm was employed as a current-collector substrate. The chemical composition of the LTO powder and SS-304 substrate is shown in Table 1. Figure 1 depicts the morphology of the LTO powder particles, as observed through scanning electron microscopy (SEM) conducted using an APREO field emission SEM (FE-SEM) from Thermo Fisher Scientific, U.S., equipped with an EDS detector. The SEM micrograph of the LTO thin-film cross-section is shown in Fig. 1(c) indicating a uniform deposition of the LTO thin film. The suspension was formulated in deionized water, comprising a 20 wt.% solid load of LTO powder and 1 wt.% of 1-Methyl-2-pyrrolidinone (NMP) from Sigma-Aldrich as an additive. Subsequently, the LTO thin-film was deposited using an Axial III high-power plasma torch

Table 1 Chemical composition of LTO thin-film and SS-304 substrate

Element	Ti	O	Cl, Si, Al	Fe	Cr	Ni	Mn	C, P, S, Si, N
LTO powder (wt.%) (Excluding Li, which could not be detected)	54.4	45.2	0.4	…	…	…	…	…
SS-304 substrate (wt.%)	…	…	…	Balance	18-20	8-11	2	1.005

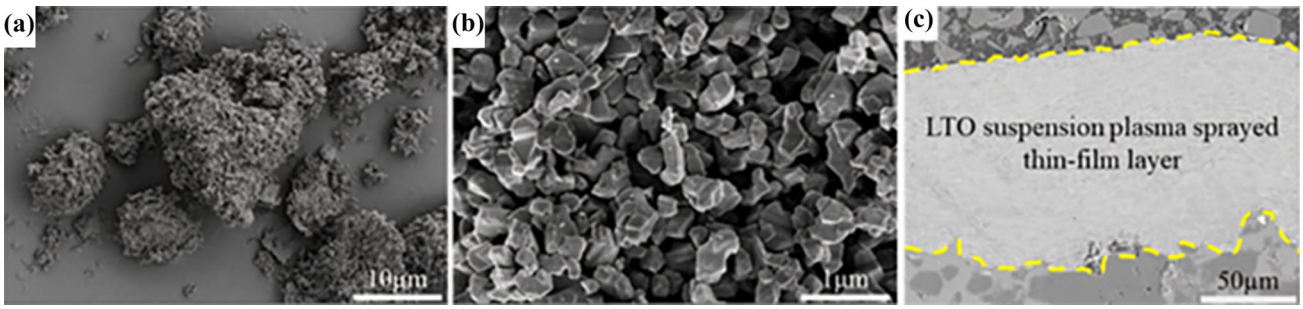

Fig. 1 SEM micrographs with (a) low and (b) high magnifications of morphology of the LTO powder, (c) Cross-sectional BSE image of LTO thin-film on substrate

Table 2 Plasma spray parameters utilized for the deposition of the LTO suspension

Suspension feed, mL/min	Total gas flow, L/min	Power, kW	Enthalpy, kJ	Number of passes
42	200	110	11	20

(Northwest Mettech Corp., Vancouver, Canada) equipped with a Nanofeed 350 suspension feed system. The SPS process parameters are shown in Table 2. Further details about this technique and the subsequent coating formation mechanisms can be found elsewhere (Ref 10, 16). The choice of the sample in this study was guided by the authors' earlier works (Ref 31), where processing conditions were optimized. This allowed for in-depth, advanced characterization on the selected sample, ensuring comprehensive insights under proven optimal conditions.

Sample preparation for synchrotron μXRD/μXRF: A focused ion beam (FIB) was used to prepare a sample from the LTO layer for micro-characterization. This process involved a Xe + ion beam at 30 kV for milling and 12 kV for carbon deposition, which attached the manipulator to the micro-sample for lift-out and mounting on a pin for x-ray measurements. As shown in Fig. 2, the preparation includes multiple steps, resulting in a sample of 250 × 200 × 40 μm. The 40 μm thickness is determined by the x-ray beam energy and material absorption. The height ensures the sample contains all layers and some substrate material. In Fig. 2(l), the yellow-dotted and red-dotted lines indicate the LTO thin-film and the SS-304 substrate, respectively.

Synchrotron μXRD and μXRF: The chemical composition and crystalline phases at the sample interface were measured using μXRF- and μXRD-contrast microscopy at the microXAS beamline, Swiss Light Source (PSI) (Ref 32) (see schematic in Fig. 3). The XRD data was acquired using the Dectris Eiger 4 M single photon counting detector (Ref 33) and XRF using 4 SDD detectors positioned around the sample. During a raster scan over the ceramic sample cross-sections, μXRD and μXRF measurements were simultaneously performed with detectors placed as shown in Fig. 3. The x-ray beam was focused to 1 μm. A sample manipulator moved the sample in 0.5 μm steps (x and y) in the plane normal to the beam with a 200 ms acquisition time per step. For more details on the procedures, see Colldeweih et al. (Ref 34). The x-ray beam wavelength was 0.6812 Å. Detection and characterization covered a 250 × 200 μm area with 1 × 1 μm pixels and 0.5 μm steps. Azimuthal integration of diffraction rings used the pyFAI Python library (Ref 35). Each integrated diffraction pattern was assigned to a pixel in the scanned area, resulting in 3000 images showing XRD intensities at specific diffraction angles. For the same area, x-ray fluorescence spectra from each pixel were recorded and analyzed using PyMca software (Ref 36) which allowed to obtain distinct images representing spatial distribution of individual elements. Both μXRD and μXRF measurements

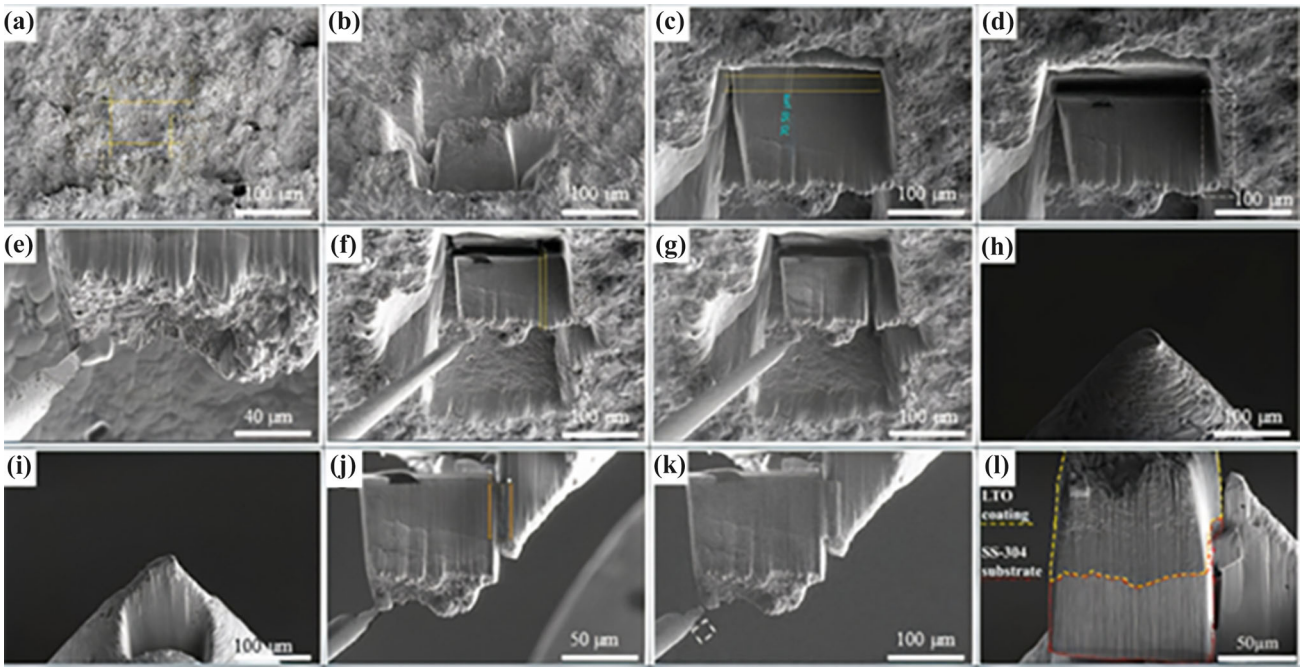

Fig. 2 FIB milling process steps: (a) Locating a region and placing milling patterns, (b) Top-down milled micro-sample, (c) Undercut to create a free-standing micro-sample, (d) Bridge holding the micro-sample in place, (e) Attaching the micromanipulator to the micro-sample by carbon deposition, (f) Removing the bridge, (g) Fully-released sample to be lifted out, (h) Tip of the pin as is, (i) FIB milling to create a suitable mounting site at the tip of the pin, (j) Mounting the micro-sample to the pin by carbon deposition, (k) Removing the manipulator, (l) Final FIB milled micro-sample ready for the synchrotron micro-characterization

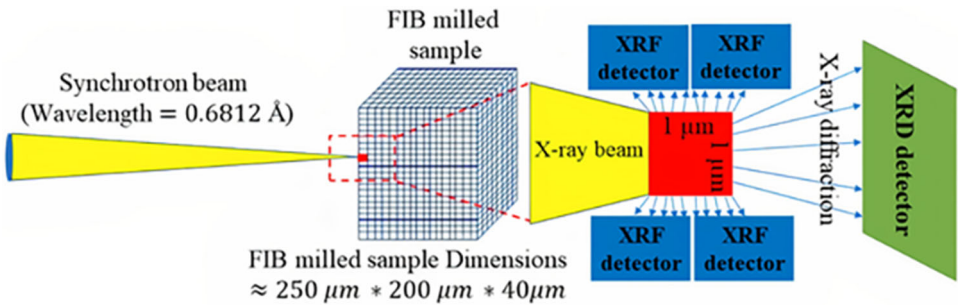

Fig. 3 Schematic illustration of the synchrotron µXRD and µXRF measurements

provide complementary information and an understanding of sample structure and composition.

ImageJ (Fiji) software (ver. 1.53q) was used to evaluate diffraction patterns from selected regions. X'Pert High Score plus software (ver. 4.9) and Topas 6 (Bruker) was used to analyze the obtained XRD patterns. The crystalline phases were identified based on Rietveld refinement.

Results and Discussion

Based on synchrotron µXRF results, the energy range of the XRF spectra at the microXAS beamline enabled imaging of the sample's chemical composition, particularly for elements with emission lines above 2 keV. Figure 4 shows the elemental distribution in the FIB-milled samples from µXRF. In Fig. 4(a), the bright distribution of Ti indicates a stable LTO thin-film on the substrate with a sharp interface, supporting µXRD findings that confirm the retention of the original $Li_4Ti_5O_{12}$ phase. Figure 4(b-e) illustrate the elemental distributions of Fe, Cr, Ni, and Mn from the SS-304 substrate, showing interdiffusion into the deposited layer. This interdiffusion within the first few microns aligns with µXRD results, which detected secondary phases like $Li_2Ti_3O_7$, Li_2TiO_3, and TiO_2, likely formed by the altered stoichiometry and oxidation states of Ti due to the presence of Fe, Cr, Ni, and Mn.

More importantly, based on synchrotron µXRD results, µXRD analysis revealed important details about phase stability and transformations in the plasma-sprayed LTO thin film. Figure 5(a-d) show cross-sectional µXRD patterns from different regions of the film, analyzed to

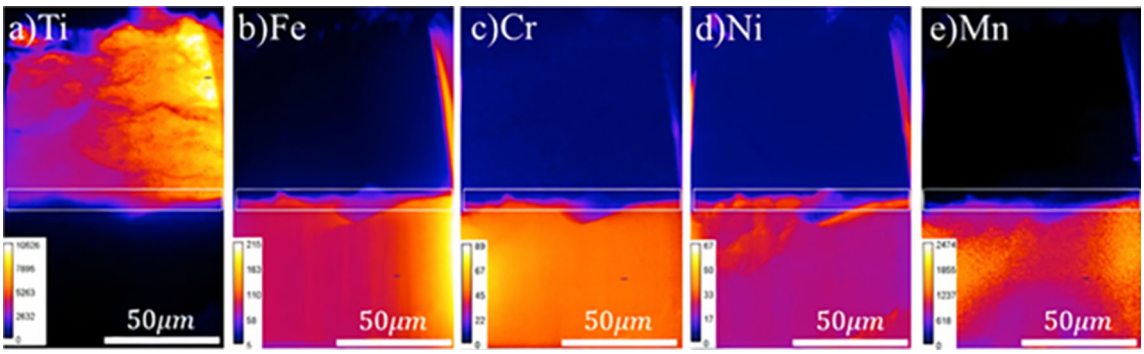

Fig. 4 elemental distribution of sample

understand phase distribution. The examined regions include: (a) LTO1, far from the interface; (b) LTO2, near the interface; (c) the LTO/substrate interface; and (d) the SS-304 substrate. The μXRD results confirm the persistence of the $Li_4Ti_5O_{12}$ (LTO) phase throughout the film, indicating its stability despite the high thermal fluxes of the SPS process. Figure 5(e) and (f) show diffraction beam intensities at angles of 11.1° and 19.3°, corresponding to the Li_2TiO_3 and bcc steel phases, respectively, illustrating their spatial distribution. Despite the dominant the presence of $Li_4Ti_5O_{12}$, the detection of secondary phases—$Li_2Ti_2O_7$, Li_2TiO_2, and TiO_2—highlights the complex thermodynamic and kinetic processes at play during film deposition. As can be seen from the phase diagram in Fig. 5(g) (red dotted line), $Li_4Ti_5O_{12}$ is an intermediate phase that can be solid-state transformed to $Li_2Ti_3O_7$, Li_2TiO_3, and TiO_2 and vice versa. The presence of $Li_2Ti_3O_7$ and Li_2TiO_3, even in regions far from the interface, suggests that partial lithium deintercalation and phase transformation occur under the extreme conditions of plasma spraying. This transformation is likely driven by the elevated temperatures, which promote the oxidation of Ti^{3+} to Ti^{4+} and result in phases with different Li/Ti ratios, such as $Li_2Ti_3O_7$ (Li/Ti = 0.67) and Li_2TiO_3 (Li/Ti = 2.0), compared to the original $Li_4Ti_5O_{12}$ (Li/Ti = 0.8). The formation of TiO_2 confined to the LTO2 region, may be attributed to localized oxidation processes where Ti^{3+} is fully oxidized to Ti^{4+}, exacerbated by oxygen ingress during deposition (Ref 8, 37, 38). Although $Li_4Ti_5O_{12}$ is the desired phase for a high-performance anode, $Li_2Ti_3O_7$ and Li_2TiO_3 phases are also shown to have good specific capacity, excellent reversibility, and cycle stability (Ref 39, 40).

The variation in cooling rates across the thin-film and substrate interface plays a crucial role in determining the final phase composition. In the LTO1 region (Fig. 5a), the μXRD pattern reveals the presence of crystalline $Li_4Ti_5O_{12}$ and $Li_2Ti_3O_7$, indicating that high-temperature conditions promote the loss of lithium and subsequent formation of lower Li/Ti ratio phases. However, the bulk film's resistance to extensive lithium loss suggests that kinetic barriers or rapid quenching may prevent widespread degradation, preserving the $Li_4Ti_5O_{12}$ phase even in thermodynamically favorable conditions for transformation.

The thermodynamics and kinetics of phase transformations and chemical reactions during plasma spraying are highly complex due to the extreme temperatures and rapid cooling rates involved. In this study, we aim to describe these phase changes and reactions using equilibrium binary phase diagrams and micro-XRD analysis. Given that oxidation is inevitable at high temperatures, lithium loss during plasma spraying is a critical factor influencing phase stability. Our findings suggest that $Li_4Ti_5O_{12}$ (LTO) can decompose into phases such as $Li_2Ti_2O_7$, Li_2O, Li_2TiO_2, and TiO_2, depending on the conditions. Previous studies also indicate that LTO decomposition occurs at elevated temperatures, particularly in oxidizing environments, with lithium loss playing a significant role in these transformations (Ref 41). Detailed reaction mechanism with equations for the phase transformation supported with thermodynamic calculations is provided in supplementary information.

The detection of Li_2TiO_3 in the LTO2 (Fig. 5b) and interface regions further supports the notion of temperature-driven phase evolution, with sufficient thermal energy available to induce solid-state transformations. Given the low thermal conductivity of LTO (1.23 W m^{-1} K^{-1}) (Ref 42), the sustained heat within the thin-film during deposition likely facilitates these transformations, allowing initially deposited $Li_4Ti_5O_{12}$ to partially convert to $Li_2Ti_3O_7$ and Li_2TiO_3. The observed TiO_2 formation, though limited, suggests that localized oxidation processes may occur, particularly in regions where thermal gradients and oxygen availability converge, leading to the complete Li loss and oxidation of Ti^{3+} to Ti^{4+}(Ref 8).

At the interface between the LTO film and the SS-304 substrate (Fig. 5c), the μXRD pattern detected significant peaks corresponding to $Li_4Ti_5O_{12}$. The high cooling rates experienced by the first few layers of molten $Li_4Ti_5O_{12}$ in

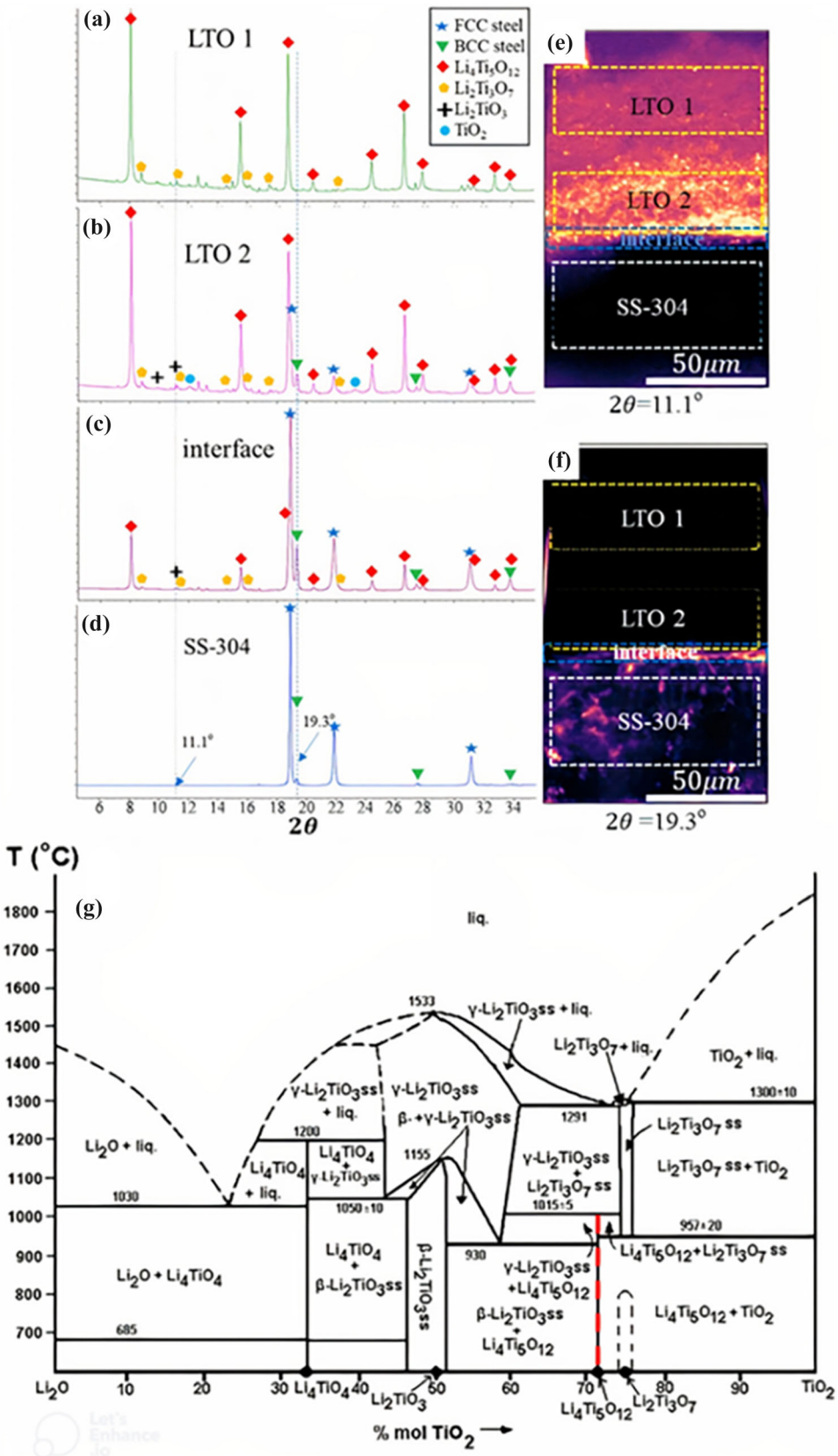

Fig. 5 XRD patterns integrated over four distinct regions: (a) LTO1, located far from the interface; (b) LTO2, positioned near the interface; (c) the interface between the LTO thin film and the substrate; and (d) the SS-304 substrate, encompassing the entire 2θ range. Two specific diffraction angles 2θ corresponding to diffraction peaks of Li_2TiO_3 and BCC steel are highlighted with dotted lines, and their corresponding images, are displayed in (e) at 2θ = 11.1° and (f) at 2θ = 19.3°, with all four regions indicated by color-coded dotted rectangles and a normalized scale bar showing values from 0 to 1. (g) The pseudo-binary Li_2O–TiO_2 phase diagram. Used with permission of Elsevier, from "Phase equilibria in the system Li_2O-TiO_2," Izquierdo, Georgina; West, Anthony R., Materials Research Bulletin, Vol 15, no. 11, 1980; permission conveyed through Copyright Clearance Center, Inc. (Ref19)

contact with the highly conductive SS-304 substrate (thermal conductivity of 14.6 W m^{-1} K^{-1} (Ref 43) appear to inhibit phase transformation, preserving the original LTO structure. However, the presence of minor peaks corresponding to $Li_2Ti_3O_7$ and Li_2TiO_3 suggests that small regions of the film may still undergo phase changes due to localized compositional inhomogeneities or slower cooling rates.

The presence of both FCC and BCC steel phases in the interface region suggests that the substrate may undergo phase transformations during SPS, likely due to interdiffusion and high thermal gradients (Ref 44). XRD mapping of crystalline phases showed a significantly higher concentration of the BCC phase near the interface compared to the substrate bulk. This is illustrated in Fig. 5(f), where the color scale indicates the BCC phase. The increased BCC phase is due to the diffusion of atoms that stabilize the FCC phase through the interface (Ref 45, 46). Elemental interdiffusion from the substrate to the LTO film may particularly be occurring, as Fe, Cr, Ni, and Mn—all present in SS-304—can migrate into the LTO layer. This diffusion can alter the local stoichiometry and phase stability within the LTO, potentially influencing the oxidation state of Ti and the formation of solid solution or secondary phases. For instance, the ionic radii of Fe^{3+} (0.65 Å), Cr^{3+} (0.62 Å), Ni^{2+} (0.69 Å), and Mn^{3+}(0.645 Å) are comparable to those of Ti^{4+}(0.61 Å) and Ti^{3+}(0.67 Å), making them potential candidates for substitution into the LTO lattice, thus forming solid solutions. These substitutions could introduce lattice strain, modify the phase stability, and influence the electrochemical properties of the LTO film. Additionally, the presence of Ni and Cr, known for their catalytic properties, could facilitate the oxidation of Ti^{3+} to Ti^{4+} (Ref 47, 48).

The μXRD and μXRF analyses not only reveal the complexity of the interfacial region between the LTO material and substrate, showing mixed phases and solid solutions due to elemental interdiffusion, but also reveal the complex interfacial region between the LTO material and substrate, highlighting mixed phases and solid solutions caused by elemental interdiffusion. This critical interfacial zone, characterized by overlapping distributions of Ti, Fe, Cr, Ni, and Mn, underscores the significant impact of these elements on the LTO anode's structural integrity and electrochemical properties. The μXRF results, which map the spatially resolved chemical composition, confirm the crucial role of substrate element interdiffusion in forming complex interfacial structures. This interplay between chemical composition and phase transformation emphasizes the need to control interfacial reactions to optimize the performance and stability of LTO-based anodes in lithium-ion batteries.

Conclusion

This study used advanced synchrotron-based μXRD and μXRF techniques to analyze phase and elemental distribution in an LTO thin-film anode, produced via suspension plasma spray (SPS) for solid-state lithium batteries. The LTO film was deposited on an SS-304 substrate, and micro-scale analysis provided insights into phase stability and interfacial interactions.

The μXRD analysis confirmed the persistence of the $Li_4Ti_5O_{12}$ phase across the film, with distinct regions (LTO1 and LTO2) exhibiting different phase compositions due to variations in thermal exposure during SPS. In LTO1, $Li_4Ti_5O_{12}$ was predominant with minor $Li_2Ti_3O_7$ formation due to lithium loss at high temperatures. Near the SS-304 substrate, rapid cooling rates preserved the $Li_4Ti_5O_{12}$ phase, while in the LTO2 region, prolonged high-temperature exposure led to the formation of additional phases like Li_2TiO_3. The μXRF together with μXRD analysis revealed elemental interdiffusion of Fe, Cr, Ni, and Mn from the SS-304 substrate into the LTO layer, resulting in increased amount of the BCC phase in steel, contributing to localized phase transformations and the formation of complex structures at the interface. The interplay between the thermal history, cooling rates, and substrate interactions was found to govern the distribution and stability of phases within the thin film.

Overall, this study demonstrates the intricate relationship between processing conditions and material properties in SPS-deposited LTO thin films. The findings highlight the need to control SPS parameters to enhance the performance and stability of solid-state lithium battery components, especially at the anode-substrate interface.

Supplementary Information The online version contains supplementary material available at https://doi.org/10.1007/s11666-025-02003-6.

Acknowledgments The authors would like to acknowledge the invaluable contributions of Stefan Björklund and Killian Clovis from University West, Trollhättan, Sweden, for their assistance with plasma spraying of the battery materials and electron microscopy for characterizing the sprayed layer.

Funding Open Access funding provided by University of Turku (including Turku University Central Hospital). This research was supported by the GREEN-BAT project (2022–2025) under the M-ERA.Net framework. The authors gratefully acknowledge the support of the Research Council of Finland and M-ERA.NET 3 from the European Commission, as well as the respective national and regional financiers from Germany and Sweden. The Swedish portion of this research, conducted at University West, Sweden, was funded by the following projects: (a) the proof-of-concept project NovelCABs, supported by the Swedish Energy Agency (Energimyndigheten, Dnr 2021-002227), and (b) the transnational M-ERA.NET 3 project Green-BAT, with backing from the European Commission, with Vinnova (the Swedish Governmental Agency for Innovation Systems)

as the national financier for Swedish participation. The Authors also acknowledge Swiss Light Source (SLS) for granting the beamtime at the microXAS beamline. This project has received funding from the European Union's Horizon 2020 research and innovation program under grant agreement No 958174.

References

1. P. Kurzweil, Gaston Planté and his Invention of the Lead–Acid Battery—The Genesis of the First Practical Rechargeable Battery, *J. Power. Sources*, 2010, **195**(14), p 4424-4434. https://doi.org/10.1016/j.jpowsour.2009.12.126
2. D. A. J. Rand and P. T. Moseley, Energy Storage with Lead–Acid Batteries, in Electrochemical Energy Storage for Renewable Sources and Grid Balancing, Elsevier, 2015, pp. 201-222. https://doi.org/10.1016/B978-0-444-62616-5.00013-9
3. J. Garche, C. Dyer, P. T. Moseley, Z. Ogumi, D. A. J. Rand, and B. Scrosati, Encyclopedia of electrochemical power sources, 2013, Newnes
4. A. B. Yaroslavtsev, I. A. Stenina, T. L. Kulova, A. M. Skundin, and A. V. Desyatov, Nanomaterials for Electrical Energy Storage, in Comprehensive Nanoscience and Nanotechnology, Elsevier, 2019, pp. 165-206. https://doi.org/10.1016/B978-0-12-803581-8.10426-6
5. M.R. Mohammadi and D.J. Fray, Low Temperature Nanostructured Lithium Titanates: Controlling the Phase Composition, Crystal Structure and Surface Area, *J. Solgel Sci. Technol.*, 2010, **55**(1), p 19-35. https://doi.org/10.1007/s10971-010-2209-6
6. M. Vijayakumar, S. Kerisit, K.M. Rosso, S.D. Burton, J.A. Sears, Z. Yang, G.L. Graff, J. Liu, and H. Jianzhi, Lithium Diffusion in Li4Ti5O12 at High Temperatures, *J. Power. Sources*, 2011, **196**(4), p 2211-2220. https://doi.org/10.1016/j.jpowsour.2010.09.060
7. E.M. Sorensen, S.J. Barry, H.-K. Jung, J.M. Rondinelli, J.T. Vaughey, and K.R. Poeppelmeier, Three-Dimensionally Ordered Macroporous Li4 Ti5 O12: Effect of Wall Structure on Electrochemical Properties, *Chem. Mater.*, 2006, **18**(2), p 482-489. https://doi.org/10.1021/cm052203y
8. X. Sun, P.V. Radovanovic and B. Cui, Advances in Spinel Li4 Ti5 O12 Anode Materials for Lithium-Ion Batteries, *New J. Chem.*, 2015, **39**(1), p 38-63. https://doi.org/10.1039/C4NJ01390E
9. S. Zhou, N. Huang, J. Yan, H. Zhang, and X. Li, High Rate Performance Li4 Ti5 O12 /N-doped Carbon/Stainless Steel Mesh Flexible Electrodes Prepared by Electrostatic Spray Deposition for Lithium-ion Capacitors, *Chem. Lett.*, 2020, **49**(3), p 337-340. https://doi.org/10.1246/cl.190886
10. A. Hasani, M. Luya, N. Kamboj, C. Nayak, S. Joshi, A. Salminen, S. Goel, and A. Ganvir, Laser Processing of Liquid Feedstock Plasma-Sprayed Lithium Titanium Oxide Solid-State-Battery Electrode, *Coatings*, 2024, **14**(2), p 224. https://doi.org/10.3390/coatings14020224
11. X. Liang, Y. Wang, X. Zhang, D. Han, L. Lan, and Y. Zhang, Performance Study of a Li4Ti5O12 Electrode for Lithium Batteries Prepared by Atmospheric Plasma Spraying, *Ceram. Int.*, 2019, **45**(17), p 23750-23755. https://doi.org/10.1016/j.ceramint.2019.08.091
12. X. Wu, X. Liang, X. Zhang, L. Lan, S. Li, and Q. Gai, Structural Evolution of Plasma Sprayed Amorphous Li4Ti5O12 Electrode and Ceramic/Polymer Composite Electrolyte During Electrochemical Cycle of Quasi-Solid-State Lithium Battery, *J. Adv. Ceram.*, 2021, **10**(2), p 347-354. https://doi.org/10.1007/s40145-020-0447-9
13. M. Oksa, E. Turunen, T. Suhonen, T. Varis, and S.-P. Hannula, Optimization and Characterization of High Velocity Oxy-fuel Sprayed Coatings: Techniques, Materials, and Applications, *Coatings*, 2011, **1**(1), p 17-52. https://doi.org/10.3390/coatings1010017
14. L. Bianchi, A.C. Leger, M. Vardelle, A. Vardelle, and P. Fauchais, Splat Formation and Cooling of Plasma-Sprayed Zirconia, *Thin Solid Films*, 1997, **305**(1–2), p 35-47. https://doi.org/10.1016/S0040-6090(97)80005-3
15. P. Kotalík and K. Voleník, Cooling Rates of Plasma-Sprayed Metallic Particles in Liquid and Gaseous Nitrogen, *J. Phys. D Appl. Phys.*, 2001, **34**(4), p 567-573. https://doi.org/10.1088/0022-3727/34/4/318
16. A. Ganvir, R.F. Calinas, N. Markocsan, N. Curry, and S. Joshi, Experimental Visualization of Microstructure Evolution During Suspension Plasma Spraying of Thermal Barrier Coatings, *J. Eur. Ceram. Soc.*, 2019, **39**(2–3), p 470-481. https://doi.org/10.1016/j.jeurceramsoc.2018.09.023
17. M. Aghasibeig, F. Tarasi, R.S. Lima, A. Dolatabadi, and C. Moreau, A Review on Suspension Thermal Spray Patented Technology Evolution, *J. Therm. Spray Technol.*, 2019, **28**(7), p 1579-1605. https://doi.org/10.1007/s11666-019-00904-x
18. C. Torre-Gamarra, M. Sotomayor, W. Bucheli, J. Amarilla, J. Sanchez, B. Levenfeld, and A. Varez, Tape Casting Manufacturing of Thick Li4Ti5O12 Ceramic Electrodes with High Areal Capacity for Lithium-Ion Batteries, *J. Eur. Ceram. Soc.*, 2021, **41**(1), p 1025-1032. https://doi.org/10.1016/j.jeurceramsoc.2020.07.049
19. G. Izquierdo and A.R. West, Phase Equilibria in the System Li2O-TiO2, *Mater. Res. Bull.*, 1980, **15**(11), p 1655-1660. https://doi.org/10.1016/0025-5408(80)90248-2
20. S. Mathiyalagan, S. Björklund, S. Johansson Storm, G. Salian, R. Le Ruyet, R. Younesi, and S. Joshi, Facile One-Step Fabrication of Li4Ti5O12 Coatings by Suspension Plasma Spraying, *Mater. Res. Bull.*, 2025, **181**, p 113111. https://doi.org/10.1016/j.materresbull.2024.113111
21. T. Zhu, M. Baeva, H. Testrich, T. Kewitz, and R. Foest, Effect of a Spatially Fluctuating Heating of Particles in a Plasma Spray Process, *Plasma Chem. Plasma Process.*, 2022, **43**, p 1-24. https://doi.org/10.1007/s11090-022-10290-y
22. K. Płatek, L. Łatka, and M. Nowakowska, The Influence of Injection Mode and Spray Distance on Wear Resistance of Al2O3+13 wt.% TiO2 Coatings, *Adv. Mat. Sci.*, 2024 https://doi.org/10.2478/adms-2024-0014

23. E. Peleg and A. Vackel, Effects of Plume Targeted Cooling on Residual Stress in Controlled Atmosphere Plasma Sprayed Coatings, *J. Therm. Spray Tech.*, 2024 https://doi.org/10.1007/s11666-024-01857-6
24. C. Wang, M. Liu, M. Thijs, F.G.B. Ooms, S. Ganapathy, and M. Wagemaker, High Dielectric Barium Titanate Porous Scaffold for Efficient Li Metal Cycling in Anode-Free Cells, *Nat. Commun.*, 2021, **12**(1), p 6536. https://doi.org/10.1038/s41467-021-26859-8
25. J. Speulmanns, A.M. Kia, K. Kühnel, S. Bönhardt, and W. Weinreich, Surface-Dependent Performance of Ultrathin TiN Films as an Electrically Conducting Li Diffusion Barrier for Li-Ion-Based Devices, *ACS Appl. Mater. Interfaces*, 2020, **12**(35), p 39252-39260. https://doi.org/10.1021/acsami.0c10950
26. A. Ghosh and F. Ghamouss, Role of Electrolytes in the Stability and Safety of Lithium Titanate-Based Batteries, *Front Mater*, 2020, **7**, p 186. https://doi.org/10.3389/fmats.2020.00186
27. H. Zhou and C. Peng, Effect of Shroud in Plasma Spraying on Chemical Composition and Thickness of Titanium Coatings, *Coatings*, 2021, **11**(4), p 446. https://doi.org/10.3390/coatings11040446
28. M. Mahrukh, S. Liu, L. Zhang, S. Husnain, C. Yang, X. Luo, and C. Li, A Study of Particle Heating and Oxidation Protection in a Modified Internally Injected Ar–H2 Atmospheric Plasma Spraying Torch, *Plasma*, 2025, **8**(1), p 5. https://doi.org/10.3390/plasma8010005
29. P. Kaskes, T. Déhais, S. J. de Graaff, S. Goderis, and P. Claeys, Micro–x-ray Fluorescence (μXRF) Analysis of Proximal Impactites: High-Resolution Element MAPPING, Digital Image Analysis, and Quantifications, in Large Meteorite Impacts and Planetary Evolution VI, Geological Society of America, 2021, pp. 171-206. https://doi.org/10.1130/2021.2550(07)
30. H.A.O. Wang, D. Grolimund, L.R. Van Loon, K. Barmettler, C.N. Borca, B. Aeschlimann, and D. Günther, Quantitative Chemical Imaging of Element Diffusion into Heterogeneous Media Using Laser Ablation Inductively Coupled Plasma Mass Spectrometry, Synchrotron Micro-x-ray Fluorescence, and Extended x-ray Absorption Fine Structure Spectroscopy, *Anal. Chem.*, 2011, **83**(16), p 6259-6266. https://doi.org/10.1021/ac200899x
31. Killian Clovis, Deposition and Characteristics of Ther-Mal Sprayed Layers as Solid-State Thin Film Battery Components," 2023, University West, Trollhättan, Sweden.
32. C.N. Borca, D. Grolimund, M. Willimann, B. Meyer, K. Jefimovs, J. Vila-Comamala, and C. David, The microXAS Beamline at the Swiss Light Source: Towards Nano-Scale Imaging, *J. Phys. Conf. Ser.*, 2009, **186**, p 012003. https://doi.org/10.1088/1742-6596/186/1/012003
33. S. Grimm, https://www.dectris.com/en/detectors/x-ray-detectors/eiger2/eiger2-for-synchrotrons/
34. A.W. Colldeweih, M.G. Makowska, O. Tabai, D.F. Sanchez, and J. Bertsch, Zirconium Hydride Phase Mapping in Zircaloy-2 Cladding after Delayed Hydride Cracking, *Materialia (Oxf)*, 2023, **27**, p 101689. https://doi.org/10.1016/j.mtla.2023.101689
35. G. Ashiotis, A. Deschildre, Z. Nawaz, J.P. Wright, D. Karkoulis, F. Emmanuel Piccac, and J. Kieffer, The Fast Azimuthal Integration Python Library: pyFAI, *J. Appl. Crystallogr.*, 2015, **48**(2), p 510-519. https://doi.org/10.1107/S1600576715004306
36. V.A. Solé, E. Papillon, M. Cotte, Ph. Walter, and J. Susini, A Multiplatform Code for the Analysis of Energy-Dispersive x-ray Fluorescence Spectra, *Spectrochim. Acta Part B At. Spectrosc.*, 2007, **62**(1), p 63-68. https://doi.org/10.1016/j.sab.2006.12.002
37. Z. Liu, Y. Huang, X. Wang, Y. Zhang, J. Ding, Y. Guo, and X. Tang, Synthesis of Defects and TiO2 Co-Enhanced Li4Ti5O12 by a Simple Solid-State Method as Advanced Anode for Lithium-Ion Batteries, *J. Mater. Sci. Mater. Electron.*, 2021, **32**(5), p 6682-6687. https://doi.org/10.1007/s10854-021-05383-x
38. A. Subhan, F. Oemry, S.N. Khusna, and E. Hastuti, Effects of Activated Carbon Treatment on Li4Ti5O12 Anode Material Synthesis for Lithium-Ion Batteries, *Ionics (Kiel)*, 2019, **25**(3), p 1025-1034. https://doi.org/10.1007/s11581-018-2633-0
39. Q. Meng, L. Wang, F. Chen, Q. Hao, and X. Sun, Preparation of Ramsdellite-type Li2Ti3O7 Hollow Microspheres with High Tap Density by Flame Melting Method as Anode of Li-Ion Battery, *Mater. Res. Bull.*, 2023, **161**, p 112166. https://doi.org/10.1016/j.materresbull.2023.112166
40. Y. Kang, Y. Xie, F. Su, K. Dai, M. Shui, and J. Shu, α-Li 2 TiO 3: A New Ultrastable Anode Material for Lithium-Ion Batteries, *Dalton Trans.*, 2022, **51**(47), p 18277-18283. https://doi.org/10.1039/D2DT03115A
41. H.A. Mosqueda and H. Pfeiffer, Kinetic Analysis of the Thermal Decomposition of Li4Ti5O12 Pellets, *Pro App Cer*, 2011, **5**(4), p 199-203. https://doi.org/10.2298/PAC1104199M
42. K. Yang, Z. Shan, X. Liu, L. Tan, and S. Wang, Study on Thermal Simulation of LiNi 0.5 Mn 1.5 O 4 /Li 4 Ti 5 O 12 Battery, *Energy Technol.*, 2021 https://doi.org/10.1002/ente.202000816
43. S.C. Chen, C.C. Wan, and Y.Y. Wang, Thermal Analysis of Lithium-Ion Batteries, *J. Power. Sources*, 2005, **140**(1), p 111-124. https://doi.org/10.1016/j.jpowsour.2004.05.064
44. J. Pelleg, Interdiffusion, 2016, pp. 69-74. https://doi.org/10.1007/978-3-319-18437-1_6
45. G.N. Irving, J. Stringer, and D.P. Whittle, Effect of the Possible fcc Stabilizers Mn, Fe, and Ni on the High-Temperature Oxidation of Co-Cr Alloys, *Oxid. Met.*, 1974, **8**(6), p 393-407. https://doi.org/10.1007/BF00603389
46. I. Shuro, S. Kobayashi, T. Nakamura, and K. Tsuzaki, Determination of α/γ Phase Boundaries in the Fe–Cr–Ni–Mn Quaternary System with a Diffusion-Multiple Method, *J. Alloys Compd.*, 2014, **588**, p 284-289. https://doi.org/10.1016/j.jallcom.2013.11.095
47. R.D. Shannon, Revised Effective Ionic Radii and Systematic Studies of Interatomic Distances in Halides and Chalcogenides, *Acta Crystallogr. A*, 1976, **32**(5), p 751-767. https://doi.org/10.1107/S0567739476001551
48. M. Mojahed, A. Gholizadeh, and H.R. Dizaji, Influence of Ti4+ Substitution on the Structural, Magnetic, and Dielectric Properties of Ni-Cu–Zn Ferrite, *J. Mater. Sci. Mater. Electron.*, 2024, **35**(18), p 1239. https://doi.org/10.1007/s10854-024-12978-7